

Crafting Spin-State Switchable Strain Profiles within $\text{Rb}_x\text{Co}[\text{Fe}(\text{CN})_6]_y@K_j\text{Ni}[\text{Cr}(\text{CN})_6]_k$ Heterostructures

John M. Cain, Ashley C. Felts, Mark W. Meisel,* and Daniel R. Talham*



Cite This: *Chem. Mater.* 2021, 33, 246–255



Read Online

ACCESS |



Metrics & More

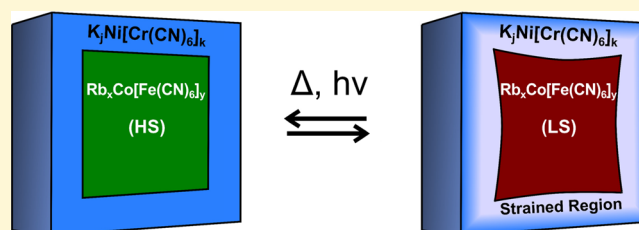


Article Recommendations



Supporting Information

ABSTRACT: Spin-transition heterostructures have shown promise for inducing large switchable stresses at the nanoscale with a volumetric work density similar to piezoelectrics, but before practical applications are feasible, how heterostructure interfaces and geometry influence the transmission of stress and, in return, how they affect the spin-transition actuator itself, must be better understood. Here, four series of cubic spin-transition Prussian blue analogue (PBA) core–shell heterostructures were developed in order to probe the scaling behavior of the strain induced in the shell by the spin transition of the core. Cubic $\text{Rb}_x\text{Co}[\text{Fe}(\text{CN})_6]_y \cdot n\text{H}_2\text{O}$ (RbCoFe-PBA) particles ranging 100–600 nm were used to prepare separate series of $\text{Rb}_x\text{Co}[\text{Fe}(\text{CN})_6]_y \cdot n\text{H}_2\text{O}@K_j\text{Ni}[\text{Cr}(\text{CN})_6]_k \cdot m\text{H}_2\text{O}$ (RbCoFe@KNiCr-PBA) core–shell particles with magnetic KNiCr-PBA shells ranging from 15 to 130 nm. A model fit to the strain-modified magnetization extracts the “strained volume” of the shell, and the results are compared with structural changes observed with powder X-ray diffraction. A linear relationship is found between the strained volume of the shell and the volume of the core for thicker shells, where the magnetic KNiCr-PBA shell is influenced to depths greater than 100 nm in response to the spin transition of the RbCoFe-PBA core. For thin shells, the relationship is more complicated, as the volume change in the actuating core and the strain it induces in the shell become interdependent and a function of shell thickness.



INTRODUCTION

Recent research applying controlled strain to materials has illuminated a large parameter space for tuning the structural and electronic properties of materials, allowing access to topological phases,^{1–8} modification of magnetic anisotropy,^{9,10} ferroelectric ordering,¹¹ phonon engineering,^{12,13} and development of engineered bandgap gradients to modify transport and magnetization.^{14–19} Strain tuning of behavior is particularly fertile in the realm of 2D materials.^{5–12,14–16} The large volume changes, sometimes as high as 10–15%, associated with magnetic spin-transition materials make them attractive candidates for actuating strain, as they can be incorporated into nanoscale or mesoscale heterostructures and switched using external stimuli such as light, temperature, or pressure.^{20–27} In fact, the volumetric work density of these spin-transition actuators can be as high as that of piezoelectric or magnetostrictive devices.^{20,28}

The elastic response of dynamic heterostructures depends on a number of factors beyond the simple choice of materials, including the structural dimensions/geometry of the system and the specific nature of the interface. At present, detailed understanding of these factors is lacking at small length scales. Previous work using core–shell heterostructures explored how interfacial strain can be used to modify electronic and phase transition behavior^{24,29–34} in either the core or the shell, often with dramatic results. However, these studies have largely focused on the strain induced in one of the components, rather

than taking a holistic view of the strained heterostructure, and therefore neglected the factors controlling the partitioning of elastic strain between the components.³⁵ For the significant stresses encountered in many spin-transition heterostructures, the strain induced in one component is determined in large part by the stiffness of the other, but the stiffnesses of both are determined not only by their chemical nature but also by the heterostructure geometry. In core–shell heterostructures, for example, the stiffness of the shell depends strongly on its thickness,^{32,35} so the geometric influences on strain propagation need to be understood. To probe this issue, a range of chemically similar core–shell particle samples were synthesized, where the size of the core is varied over a moderate range allowing heterostructures with the same core:shell molar ratios, but different shell thicknesses, to be studied so the effect of shell stiffness can be isolated.

Prussian blue analogue (PBA) heterostructure nanoparticles offer an ideal platform with which to study the scaling behavior. Spin-transition materials are known to be sensitive to

Received: September 8, 2020

Revised: November 28, 2020

Published: December 16, 2020



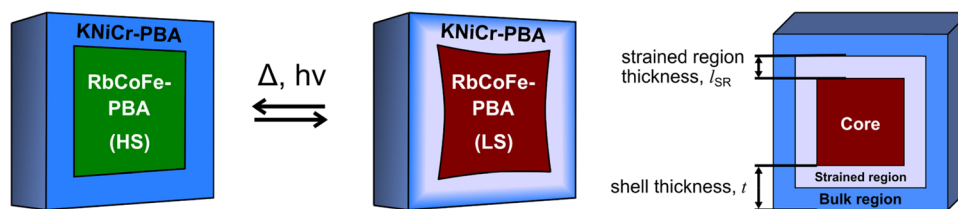


Figure 1. Schematic depicting the RbCoFe@KNiCr-PBA heterostructure and the strain induced in the KNiCr-PBA shell as a result of the RbCoFe-PBA CTIST, left. On the right, the components of the three-component model, used for interpretation of the magnetic data, are sketched.

Table 1. Particle Dimensions

	sample composition ^a	core size ^b (nm)	shell thickness ^c (nm)
1	Rb _{0.48} Co[Fe(CN) ₆] _{0.83} ·4.3H ₂ O	124 ± 14	
1@19-nm	1@{K _{0.31} Ni[Cr(CN) ₆] _{0.77} } _{1.18} ·9.8H ₂ O	124 ± 14	19 ± 3
1@33-nm	1@{K _{0.32} Ni[Cr(CN) ₆] _{0.77} } _{2.57} ·17H ₂ O	124 ± 14	33 ± 3
1@51-nm	1@{K _{0.22} Ni[Cr(CN) ₆] _{0.74} } _{5.00} ·28H ₂ O	124 ± 14	51 ± 5
2	Rb _{0.47} Co[Fe(CN) ₆] _{0.82} ·4.5H ₂ O	325 ± 34	
2@27-nm	2@{K _{0.16} Ni[Cr(CN) ₆] _{0.72} } _{0.52} ·6.9H ₂ O	325 ± 34	27 ± 7
2@69-nm	2@{K _{0.16} Ni[Cr(CN) ₆] _{0.72} } _{1.86} ·13H ₂ O	325 ± 34	69 ± 7
2@108-nm	2@{K _{0.15} Ni[Cr(CN) ₆] _{0.72} } _{3.68} ·21H ₂ O	325 ± 34	108 ± 8
3	Rb _{0.46} Co[Fe(CN) ₆] _{0.82} ·4.5H ₂ O	544 ± 138	
3@63-nm	3@{K _{0.12} Ni[Cr(CN) ₆] _{0.71} } _{0.86} ·8.7H ₂ O	544 ± 138	63 ± 13
3@94-nm	3@{K _{0.15} Ni[Cr(CN) ₆] _{0.72} } _{1.42} ·11H ₂ O	544 ± 138	94 ± 7
3@129-nm	3@{K _{0.12} Ni[Cr(CN) ₆] _{0.71} } _{2.16} ·15H ₂ O	544 ± 138	129 ± 7
4	Rb _{0.19} Co[Fe(CN) ₆] _{0.73} ·2.9H ₂ O	122 ± 12	
4@15-nm	4@{K _{0.19} Ni[Cr(CN) ₆] _{0.73} } _{0.67} ·5.8H ₂ O	122 ± 12	15 ± 5
4@29-nm	4@{K _{0.13} Ni[Cr(CN) ₆] _{0.71} } _{1.78} ·10H ₂ O	122 ± 12	29 ± 5
4@52-nm	4@{K _{0.08} Ni[Cr(CN) ₆] _{0.69} } _{4.49} ·20H ₂ O	122 ± 12	52 ± 5

^aSample compositions as determined by ICP-AES and TGA. ^bUncertainty in core size corresponds to standard deviation in particle distribution.

^cUncertainty in shell thickness corresponds to 95% confidence interval.

particle size^{36–41} and interface quality,^{42–44} variables that can be well controlled using the PBA platform. PBAs are coordination polymers that form extended networks of metal ions bridged by cyanide ligands, and core@shell heterostructures of PBAs can routinely be synthesized with polydispersities of 5–6% without the use of surfactants, which might compromise the heterostructure interface.^{29,45–47} Charge-stabilized colloidal suspensions of PBA particles allow for the controlled addition of a shell,⁴⁵ composed of another structurally similar but chemically different PBA, with epitaxy determined by the lattice mismatch between the core and shell.⁴⁴ In this study, Rb_xCo[Fe(CN)₆]_y·nH₂O (RbCoFe-PBA) is used as the spin-transition-active core, capable of undergoing a charge-transfer induced spin transition (CTIST) in response to light, temperature, or pressure changes. Specifically, the metal ions that make up the framework nodes, Co and Fe, can exist as either Co^{II}(⁴T_{1g})-NC-Fe^{III}(²T_{2g}) pairs or as Co^{III}(¹A_{1g})-NC-Fe^{II}(¹A_{1g}) pairs, referred to as high-spin (HS) and low-spin (LS), respectively, with the HS pairs transitioning to LS upon cooling just below room temperature. Additionally, at temperatures below 150 K, although the LS state is the low-temperature ground state, RbCoFe-PBA can be photoexcited to a metastable HS state, analogous to the LIESST effect in spin crossover compounds.^{48–50} This transition from LS to HS involves a reduction in the Co-N bond order, resulting in an increase in the RbCoFe-PBA cubic lattice parameter (*a*) from 9.96 to 10.3 Å and a substantial (~10%) increase in the unit cell volume.

The PBA used as the shell in this study is K_iNi[Cr(CN)₆]_k·mH₂O (KNiCr-PBA), which, with a lattice parameter of 10.45 Å, grows epitaxially on the surface of the HS RbCoFe-PBA

particles. Zentková et al.⁵¹ showed that several PBAs, including KNiCr-PBA, exhibit a dramatic pressure-induced change in the magnetization process. In the case of KNiCr-PBA, the magnetization under pressure saturates at a higher applied field than it does under ambient pressure. In low magnetic fields, this difference manifests as a pronounced change in the magnetization of the KNiCr-PBA as a function of pressure or strain, which is exploited here to allow the structural strain in the KNiCr-PBA shell to be measured with the high sensitivity characteristic of superconducting quantum interference device (SQUID) magnetometers. In this study, three different RbCoFe-PBA core sizes between 100 and 600 nm were synthesized, each with three KNiCr-PBA shell thicknesses between 15 and 130 nm. SQUID magnetometry and synchrotron powder X-ray diffraction (PXRD) were then used to characterize the scaling behavior of these spin-transition heterostructures. A model was developed and fit to the magnetic data, which was then tested for consistency using structural strain data, obtained by fitting the positions and linewidths of the PXRD diffraction peaks.

The results indicate that the volume of the shell strained by the spin transition of the core (the “strained region,” see Figure 1) is linearly dependent on the core volume for thick shells. For thin shells, the situation is more complex. Whereas the volume change of the core during the spin transition is constant for thick shells, for the thinner, less-rigid shells, the volume change in the core becomes dependent on the thickness of the shell. Here, the “strain depth” (the distance from the interface beyond which the shell is unaffected by the spin transition of the core) acts as the transition point from thin-shell to thick-shell behavior. The consequence of this

nonlinear behavior is that for a given shell material, the maximum shell volume which can be affected by each core is determined exclusively by the core size, but the approach to this maximum is determined by the properties of both the core and the shell. These results also have interesting implications for heterostructures composed of spin-transition particles dispersed in a solid matrix.

EXPERIMENTAL METHODS

Synthesis. All reactions were performed at ambient temperature and pressure, open to air. Three different sizes of RbCoFe-PBA cores were synthesized (details in [Supporting Information](#)), characterized by their mean side length: 124 nm (Sample 1), 325 nm (Sample 2), and 544 nm (Sample 3). One additional set of 122-nm particles was used for the synchrotron PXRD study (Sample 4). Sample details of cores and core-shell particles (represented as “RbCoFe-PBA core sample@KNiCr-PBA shell thickness,” e.g., 1@19-nm) are provided in [Table 1](#). Chemical reagents were purchased from Sigma-Aldrich and used as received, with exception of the potassium hexacyanochromate, which was synthesized using standard methods.⁵² Deionized water was used as solvent for all syntheses.

Characterization. Fourier transform infrared spectroscopy (FTIR) was performed on a Nicolet 6700 Thermo Scientific spectrophotometer, taking 32 scans per spectrum between 400 and 4000 cm^{-1} with a resolution of 1 cm^{-1} . Samples were drop-casted onto the face of a pressed KBr pellet by dispersing 1 mg of powder in acetone using an ultrasonic bath and dropping the dispersion onto the preformed pellet.⁵³ The spectrum of the pure KBr pellet before drop-casting is taken as a background reference. Transmission electron microscopy (TEM) was performed on either a JEOL-2010F high-resolution TEM at 200 kV or a Hitachi H-7000 TEM operating at 110 kV. The TEM samples were prepared by dropping 120 μL of an acetone suspension containing 0.25 mg of powder onto the grid (carbon film on a holey carbon support film, 400 mesh, Cu, from Ted-Pella, Inc.). Energy-dispersive X-ray spectroscopy (EDS) was performed with an Oxford Instruments EDS X-ray Microanalysis System coupled to the high-resolution TEM (HRTEM) microscope. The EDS linescan mode was used to determine the composition profile of the core-shell particles. Inductively coupled plasma-atomic emission spectroscopy (ICP-AES) was performed on an Agilent Technologies VARIAN VISTA RL simultaneous spectrometer with a CCD-detector. Standard solutions of 100, 10, 1, and 0 ppm concentrations for each element being measured were prepared from 1000 ppm standard solutions obtained from Fluka Analytical. Details on the method used to produce solutions for compositional analysis with ICP-AES can be found in the [Supporting Information](#). TGA was performed on a TA Instruments Q5000 TGA using a Pt pan and 10 mL/min N_2 purge gas flow. The temperature was scanned from ≈ 20 to 600 $^\circ\text{C}$ at 10 $^\circ\text{C}/\text{min}$. Chemical formulas are based on the metal compositions from ICP-AES as well as the mass fraction lost in the first thermal event observed via TGA. Alkali cation content was determined based on electroneutrality. The particle size distribution is determined from the size measurements of a minimum of 150 particles from TEM images taken from multiple regions of the grid. The side length measurements were made using the ImageJ imaging software.⁵⁴ The particle size is reported as either the average particle side length or the root-mean-cube (RMC) side length, along with the respective standard deviation. To calculate the RMC particle size, the measured side length of each particle was cubed, then the average of these values was taken, and the RMC is the cube root of this average. The average shell thickness is defined as half of the difference between the arithmetic mean of the core-shell particles and that of the cores. Magnetometry was performed using a commercial SQUID magnetometer (Quantum Design MPMS-XL7). The optical measurements were performed with two tape disks: one disk consists of approximately 0.5 mg of the powder sample sandwiched between two pieces of Scotch Magic tape. These two disks were mounted in a homemade quartz-glass optic sample rod connected to a Quartzline tungsten halogen lamp (400–2200 nm). The mass of sample was

determined by normalizing the dark field-cooled magnetization in the disks to a larger amount of the same sample in a gel cap inside a drinking straw in a commercial sample rod. The dark field-cooled temperature dependence of the magnetization was measured while warming from 2 to 300 K in an applied field of 100 G, after cooling from 300 K in 100 G at 1 K/min. The sample was then field-cooled the exact same way to 5 K, where isothermal light irradiation in 100 G was performed for 4 h. After 4 h, irradiation was ceased, and the light state established. The field-cooled magnetization of the light state was measured after waiting 1 h in the dark at 5 K using the same method described for the dark field-cooled measurements. Synchrotron PXRD data were collected at beamline 17-BM at the Advanced Photon Source at Argonne National Laboratory. A flat-panel amorphous-Si area detector was positioned 500 mm from the sample. Calibration was performed using $\text{Na}_2\text{Al}_2\text{Ca}_3\text{F}_{14}$ (NAC). Samples were loaded into borosilicate capillaries (0.1 mm i.d.) and exposed to X-rays of $\lambda = 0.72768 \text{ \AA}$ for no less than 5 s while the capillary was rocked a total of 5° . Temperature was regulated using an Oxford Cryosystems Cryostream nitrogen blower. Data were collected as temperature was ramped from 300 to 100 K at 2 K/min. After allowing for 30 min for equilibration at 100 K, the samples were irradiated using a MEIJI FL-150 dual fiber optic source (21 V, 150 W) for at least 30 min and up to 3 h. Irradiation was continued until the transition completed. Data were then collected while ramping temperature back to 300 K at 2 K/min, except for Samples 4@15-nm and 4@52-nm, where the temperature was held at 135 and 125 K, respectively, before warming to 300 K at 2 K/min. Diffraction images were integrated using GSAS-II, based on the NAC standard.⁵⁵ Williamson–Hall linewidth analysis was performed using FullProf Suite⁵⁶ by fitting a pseudo-Voigt function to each peak, constraining η to physically meaningful values and using the NAC profile to find the instrumental broadening.

RESULTS

Sample Composition. [Table 1](#) summarizes the sample compositions and dimensions for the four series of RbCoFe@KNiCr-PBA particles, determined using ICP-AES, TGA, and TEM. The seed-particle growth method⁴⁵ ensures that the core composition and core-shell interface for all particles in a series is identical.

The core-shell particles are abbreviated using the core@shell nomenclature, representing the core by the $\text{Rb}_x\text{Co}[\text{Fe}(\text{CN})_6]_y \cdot n\text{H}_2\text{O}$ sample numbers, 1–4, and the shell by the thickness, in nm, of the $\text{K}_m\text{Ni}[\text{Cr}(\text{CN})_6]_l \cdot m\text{H}_2\text{O}$ shell, for example 1@19-nm. [Table 1](#) also displays the shell thickness for each sample and the 95% confidence interval for the shell thickness (see [Supporting Information](#)). The dimensions of the “small cores” used for the magnetometry (Sample 1) are similar to those for the synchrotron PXRD sample (Sample 4) within uncertainty limits, and generally the sample compositions are all quite similar. Characteristic TEM images as well as core-size histograms for Samples 1, 2, and 3 are shown in [Figure S1](#), and the images show that the shape of the cores is nearly cubic. TEM images also show a clear contrast between core and shell for the heterostructure nanoparticles, as seen in [Figure 2](#). EDS linescans were used to analyze the core-shell morphology for each series, and the linescan profiles for

Samples 1@19-nm, 2@27-nm, and 3@63-nm are shown in [Figure S2](#). The EDS elemental profiles for each series are characteristic of core-shell particles (see [Supporting Information](#)).

Magnetometry. Magnetometry was performed on each series, 1@(19, 33, 51-nm), 2@(27, 69, 108-nm), and 3@(63, 94, 129-nm), as well as the bare-cores 1, 2, and 3. [Figure 3](#) shows the molar magnetization for 1@19-nm, before and after white-light irradiation, with plots for the other core-shell samples shown in [Figure S3](#). The field-cooled dark data

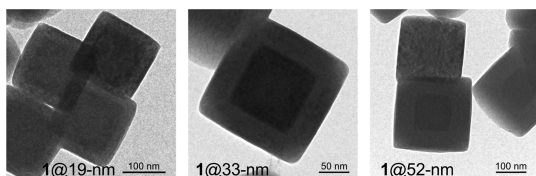


Figure 2. TEM images of RbCoFe@KNiCr-PBA Samples 1@19-nm, 1@33-nm, and 1@51-nm. The contrast between core and shell can be seen clearly.

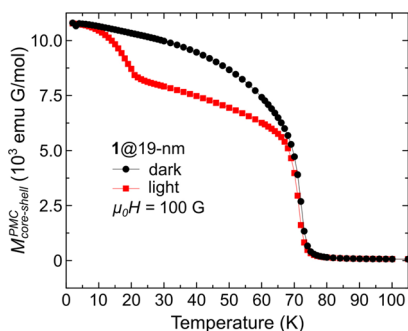


Figure 3. Field-cooled magnetization as a function of temperature for 1@19-nm, in the dark and after white-light irradiation. Data for the light state are taken with the lamp turned off, following a 4 h irradiation at 5 K. Dark and light data sets were collected while warming.

(before irradiation) show the ferromagnetic ordering of the KNiCr-PBA at approximately 70 K, and for some of the samples, the ferrimagnetic ordering at 15 K of the HS Co^{II}-NC-Fe^{III} pairs, if present (see Supporting Information for determination of CTIST-active fraction in RbCoFe-PBA cores as well as the field-cooled molar magnetization plots for the uncoated cores, Figure S4). After irradiation, there is a substantial increase in the magnetization of the core in all samples, as well as an increase in the magnetic ordering temperature of the core, as seen previously in similar samples.⁵⁷ The KNiCr-PBA, however, exhibits a decrease of magnetization as a result of the irradiation, which has been previously correlated with relief of structural strain in the shell as the core undergoes its photoinduced CTIST.⁵⁸

Structural Characterization. In order to study the change in structural strain associated with the photoinduced CTIST, synchrotron PXRD was used to study the series 2@(27, 69, 108-nm) and 4@(15, 29, 52-nm). The high brilliance associated with synchrotron radiation results in peak widths determined primarily by the sample crystallinity rather than by the X-ray optics, as is common when using laboratory sources. Each sample was measured while cooling from 300 to 100 K, and the thermal CTIST can be observed in the diffraction data as a shift in the RbCoFe-PBA peaks to higher values of 2θ between 250 and 200 K (Figure S4) as the core contracts. The reflections, in addition to shifting, became significantly broader as a result of the structural distortion in the heterostructure (Figure 4). The peak positions and profiles are largely restored to the room-temperature values upon irradiation with white light at 100 K, which establishes the metastable photoexcited HS state of the RbCoFe-PBA.

DISCUSSION

The field-cooled magnetization-versus-temperature plots show a substantial difference between the dark and light-induced

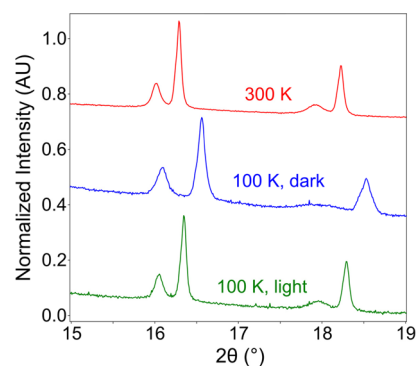


Figure 4. Detail plot of (400) and (420) reflections for 2@27-nm. The more intense lines in each pair arise from the RbCoFe-PBA core. The peak shift due to the thermal CTIST in the core upon cooling to 100 K is clearly evident, as is the effect of the strain of the thin-shell KNiCr-PBA reflection profiles. This strain is largely relieved and the peaks return to their original position after irradiation at 100 K.

response, not just in the magnitude of the KNiCr-PBA magnetization, but in its temperature dependence as well. The dark-state and photoexcited-state data bear striking resemblance to the field-cooled magnetization of thin NiCr-PBA films oriented parallel and perpendicular to the field.⁵⁹ In the earlier thin-film study, the differences in magnetization are driven by the shape anisotropy, which produces a hard axis normal to the plane of the film and an easy plane contained within the film. Similarly, for the photoinduced magnetization studied here, there is an accompanying change in the anisotropy, which has been identified as the source of the magnetization decrease in KNiCr-PBA heterostructures.⁶⁰ However, in order to extract further information about the strain behavior in the shell, a model is needed to fit the magnetic response to the strain, which is introduced next. A guide to the terms and abbreviations used in discussing this model is provided in Table S1.

Magnetic Determination of the Strained-Region Volume. The finite strain propagation length in the shell allowed Risset et al.⁴⁷ to treat the RbCoFe-PBA core, the strained region of the shell adjacent to the core–shell interface, and the unstrained (bulk-like) region of the shell as separate components of a three-component model (Figure 1). Within the framework of this early model, the change in magnetization per-mol-core (PMC) between the dark state (dark) and the photoexcited state (PX) is attributed exclusively to the core and strained regions (SR) of the shell, since the unstrained region of the shell behaves like single-phase KNiCr-PBA and shows no photomagnetism, yielding:

$$M_{\text{shell,PX}}^{\text{PMC}} - M_{\text{shell,dark}}^{\text{PMC}} = \Delta M_{\text{shell}}^{\text{PMC}} = \Delta M_{\text{SR}}^{\text{PMC}} \quad (1)$$

$$\Delta M_{\text{core-shell}}^{\text{PMC}} = \Delta M_{\text{shell}}^{\text{PMC}} + \Delta M_{\text{core}}^{\text{PMC}} \quad (2)$$

If the photoinduced changes in the magnetization of the RbCoFe-PBA core are unaltered by the presence of a shell, then the last term in eq 2 can be calculated from the known stoichiometry of the core–shell particles, and the change in the magnetization of the strained region upon exposure to light can be determined by subtracting the measured photoresponse of the uncoated cores:

$$\Delta M_{\text{shell}}^{\text{PMC}} = \Delta M_{\text{core-shell}}^{\text{PMC}} - \Delta M_{\text{uncoated cores}}^{\text{PMC}} \quad (3)$$

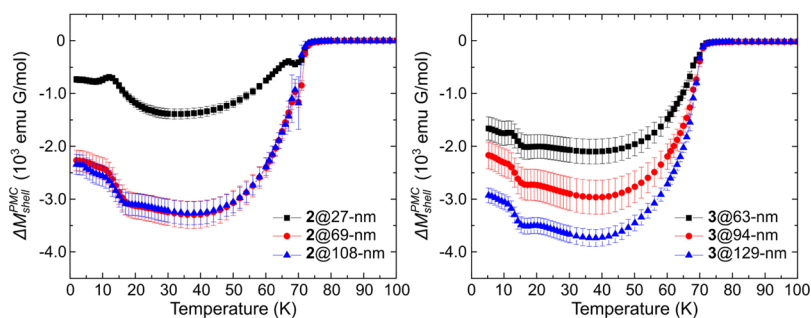


Figure 5. ΔM_{shell} , per-mol-RbCoFe-PBA, $\Delta M_{\text{shell}}^{\text{PMC}}$ for the 325-nm core series (2@27, 69, 108-nm) and the 544 nm core series (3@63, 94, 129-nm). For the 325 nm core series (left), the $\Delta M_{\text{shell}}^{\text{PMC}}$ values for the 69 nm-thick shell lie on top of those for the 108 nm shell, indicating a strained-region thickness between 27 and 69 nm. For the 544 nm core series (right), the $\Delta M_{\text{shell}}^{\text{PMC}}$ data for the 94 nm and 129 nm-thick shells differ, signifying a strained-region thickness more than 94 nm.

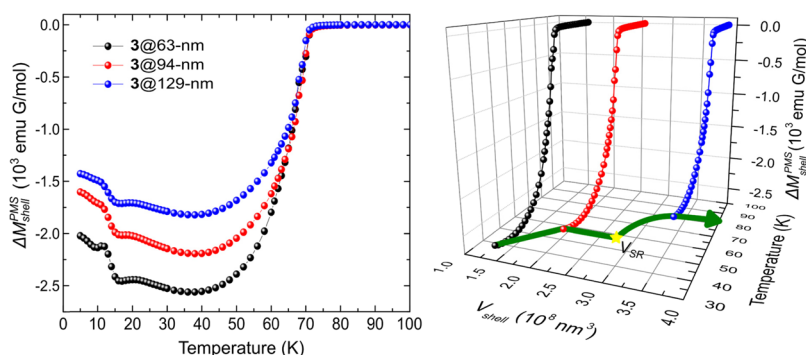


Figure 6. ΔM_{shell} , per-mol-KNiCr-PBA, $\Delta M_{\text{shell}}^{\text{PMS}}$, as a function of temperature (left), and as a function of temperature and shell volume (right) for the 544-nm cores series (3@63, 94, 129-nm). Also depicted on the right are the application of the piecewise model to the 30 K data as described in the text and the estimate of the strained-region volume (V_{SR}). The values of V_{shell} were calculated as the difference between the average volume of the core–shell particle and the average volume of the uncoated core using the RMC particle sizes, which for Samples 1, 2, and 3 are 125, 328, and 575 nm.

The utility of eq 3 lies in its ability to qualitatively distinguish between the strained region and bulk-like region of the shell. If plots of $\Delta M_{\text{shell}}^{\text{PMC}}$ -versus-temperature, T , for two different shell thicknesses are compared, the difference indicates additional strained-region material was added when going from one shell thickness to the next, but if no strained-region material was added, the two plots of $\Delta M_{\text{shell}}^{\text{PMC}}$ versus T will lie on top of each other. Figure 5 and Figure S5 show the $\Delta M_{\text{shell}}^{\text{PMC}}$ -versus- T plots for each of the samples. For Samples 2@(27, 69, 108-nm) in Figure 5, the measurements for the two thickest shells lie on top of one another, indicating a strained-region thickness between 27 and 69 nm, in good agreement with earlier estimates of 43 nm for a 347 nm core.⁵⁸ For the other samples, however, none of the plots are coincident, so only lower bounds on the strained-region thickness can be obtained. For the smaller cores series, 1@(19, 33, 51-nm), this bound is 33 nm, and for the largest cores, 3@(63, 94, 129-nm), it is 94 nm.

An interesting feature seen in several of the $\Delta M_{\text{shell}}^{\text{PMC}}$ -versus- T plots is a sharp dip near the KNiCr-PBA ordering temperature of ≈ 72 K. This feature is due to a reduction in the T_c of the KNiCr-PBA shell after light irradiation, which Knowles et al.⁶¹ attributed to a strain-induced change in the superexchange. That this feature is much more pronounced in the thinnest shells indicates the strain in the KNiCr-PBA shell at the interface is decreasing with increasing shell thickness (noting that $\Delta M_{\text{shell}}^{\text{PMC}}$ is normalized PMC, so differences between the dark and photoexcited state are not diluted upon addition of more shell material). This dependence of the strain on the

shell thickness is explored in greater detail in the Structural Analysis section. Finally, the $\Delta M_{\text{SR}}^{\text{PMC}}$ -versus- T plots, which should have no contribution from the core, display features at temperatures characteristic of the RbCoFe-PBA ordering temperature, below which the confidence intervals for the data values become quite large. These features are likely reflective of the breakdown of the assumption made in eq 3, as the structural stress at the interface has non-negligible effects on the photomagnetism of the core. However, since the analysis is complicated by the uncertainty in this region, only the data above the RbCoFe-PBA ordering temperature (≈ 20 K) are used in the quantitative analysis that follows, where the shell is magnetically ordered but the core is not, so contributions from the core to the magnetization are minor.

Further extensions of the three-component model by Felts et al.⁵⁸ allowed a quantitative estimation of the volume of the strained region from the depth profile for the magnetization of the photoexcited state per mol of core–shell, $M_{\text{shell, PX}}^{\text{per mol core-shell}}$. However, because the strain is largely relieved in the photoexcited state, this approach was later found to be a relatively insensitive probe of the strained region. A new approach is described here, based on ΔM_{shell} . In contrast to the treatment above and in Figure 5 and Figure S5, the value of ΔM_{shell} is normalized per-mol-shell (PMS) rather than to the moles of core, and will be denoted $\Delta M_{\text{shell}}^{\text{PMS}}$. This treatment allows a more sensitive determination of the strained-region volume, by fitting the effective dilution of the photoactive strained region while unstrained and non-photoactive bulk-like material is added when the shell is made thicker. More

restrictive constraints can be placed on the fits because simple dilution is such a well-defined relationship. Whereas $\Delta M_{\text{shell}}^{\text{PMC}}$ can be thought of as the total photoinduced change in the magnetization of the KNiCr-PBA shell, $\Delta M_{\text{shell}}^{\text{PMS}}$ provides the average molar change in magnetization for the KNiCr-PBA material.

The plots for $\Delta M_{\text{shell}}^{\text{PMC}}$ as a function of temperature are presented in Figure 6 and Figure S6. Neglecting the temperature region associated with the magnetically ordered RbCoFe-PBA ($T < 20$ K), all the plots now show the data in the opposite order to that in Figure 5 ($\Delta M_{\text{shell}}^{\text{PMC}}$ vs T), with the thinnest shells showing the greatest decrease in magnetization PMS. Using the three-component model, and the rationale developed above, $\Delta M_{\text{shell}}^{\text{PMS}}$ is expected to be represented by a piecewise function that depends on shell thickness, t :

$$\Delta M_{\text{shell}}^{\text{PMS}} = \begin{cases} \Delta M_{\text{SR}}^{\text{PMS}}(t), & | t < l_{\text{SR}} \\ \Delta M_{\text{SR}}^{\text{PMS}}(l_{\text{SR}}) \times \frac{V_{\text{SR}}}{V_{\text{shell}}}, & | t > l_{\text{SR}} \end{cases} \quad (4)$$

In eq 4, l_{SR} is the strained-region thickness, V_{SR} is the volume of the strained region, and V_{shell} is the volume of the shell. The explicit dependence of $\Delta M_{\text{SR}}^{\text{PMS}}$ on t for shells with $t < l_{\text{SR}}$ is reflected in the data plotted in Figure 6, where none of the plots are coincident, despite the two thinnest shells for the largest core series (Figure 5) being composed exclusively of strained-region material. A similar situation arises for the smallest core series (Figure S5). In other words, for heterostructures in which the entire shell becomes strained, the change in magnetization per mole of strained shell changes as the thickness changes. A dependence on t also explains the observation that the perturbation of the superexchange disappears for thick shells. However, $\Delta M_{\text{SR}}^{\text{PMS}}(t)$ for $t < l_{\text{SR}}$ was not modeled here, as not enough thin-shell data are available to quantitatively determine the relationship between the strain and the decrease in magnetization. Logically, though, the shell strain profile must remain constant for all shell thicknesses greater than the strain depth, and so the piece of eq 4 corresponding to $t > l_{\text{SR}}$ can still be used to solve for the volume of the strained region by estimating $\Delta M_{\text{SR}}^{\text{PMS}}(t)$ at l_{SR} . The value of $\Delta M_{\text{shell}}^{\text{PMS}}$ for the medium-shell sample is used as this estimate, justified by the sharp reduction in volumetric change in $\Delta M_{\text{shell}}^{\text{PMC}}$ with increasing shell thickness for each of the series, represented in Figure 5 as coincident plots for 2@69-nm and 2@108-nm, and supported by the structural strain profiles described later.

The values of $\Delta M_{\text{shell}}^{\text{PMS}}$ measured for the three shell thicknesses in each series were used to calculate V_{SR} using eq 4, as depicted graphically on the right-hand side of Figure 6. Specifically, the volume of the strained region is identified as the volume at which the value of $\Delta M_{\text{shell}}^{\text{PMS}}$ from the medium-shell sample can be diluted with bulk material to give the observed value for the thickest-shell sample. The values of V_{SR} obtained in this way for each series are plotted against core volume in Figure 7. The excellent linear correlation indicates the strained-region volume is directly proportional to the core volume, with the proportionality constant $V_{\text{SR}}/V_{\text{core}}$ equal to 1.70. The linearity of this relationship implies the entire three-component system scales in this size regime, and the proportionality constant is expected to be characteristic of the relative elastic properties of the core and shell, with softer shells yielding a smaller value.⁶² While the value of the vertical

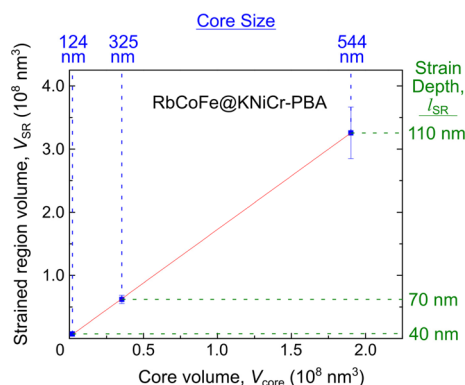


Figure 7. Strained-region volume, V_{SR} , as determined from fits to $\Delta M_{\text{shell}}^{\text{PMS}}$ per-mol-KNiCr-PBA plots, for each of the three core sizes in the study (Samples 1, 2, and 3). Linear regression yields an excellent fit to the observed trend ($R^2 > 0.99$), suggesting that the volume of the strained region is directly proportional to the core volume in the heterostructure. Along the top, the corresponding core size is indicated, which allows the strain depth (l_{SR}) to be calculated, shown along the right-hand axis.

intercept is not significantly different from zero, extrapolating to smaller core sizes can yield unphysical conclusions, since the plot becomes increasingly insensitive at small core volumes. The results in Figure 7 were obtained using the 30 K data points for each of the samples, but Figure S7 shows the near-independence of the strain depth/strained volume determination on temperature, if analyzed between the magnetic ordering temperatures of the core and the shell. A better appreciation for the scaling behavior of the strain comes from conversion of the strained-region volume into a strain depth, and these strain depths are indicated along the right-hand side of Figure 7. These strain depths are roughly 40, 70, and 110 nm for the small, medium, and large core series studied here. An important result is the realization that the magnetization of the KNiCr-PBA can be affected to a depth of 110 nm or beyond by interfacial strain, a significant distance from the interface, which is attributable to the flexibility of the KNiCr-PBA shell and the strength of the interfacial coupling.

Structural Evidence in Support of the Magnetic Model. The variable-temperature synchrotron PXRD results were analyzed to verify that the depth of changes in the magnetization of the shell correlates with the structural strain depth. Two series were analyzed, the medium-sized cores from above, 2@(27, 69, 108-nm), and a new series, 4@(15, 29, 52-nm), analogous to the small-core series studied in the magnetometer. Sequential refinement of the cubic lattice parameters for core and shell was performed after an initial Pawley refinement to fit the reflection profiles. The fitted lattice parameters are plotted versus temperature for both series in Figures S8 and S9. The plots show the photo-excitation process is not strictly reversible,⁶³ so analysis of the structural strain is restricted to the dark-state data.

The strain is quantified first by analyzing the change in the cubic lattice parameters (Δa) of both the core and the shell resulting from the thermal CTIST, which are plotted as a function of shell thickness in Figure 8. This Δa value is proportional to the canonical strain, $\Delta l/l$. The decrease in Δa for the core with increasing shell thickness matches what was seen previously in similar heterostructures^{47,58} and arises from the increasingly restricted contraction of the core as the shell thickness increases. Recalling the model developed for the

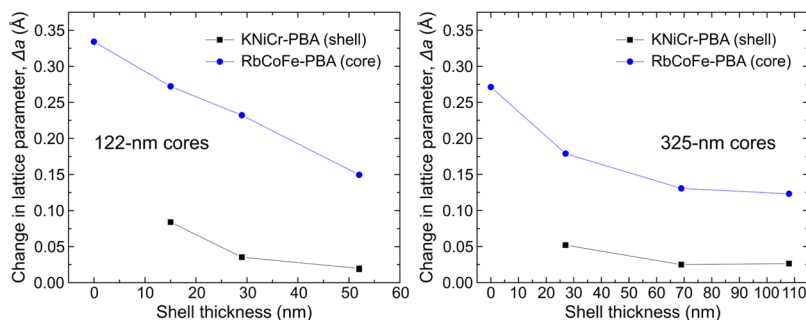


Figure 8. Reduction in the cubic lattice parameter determined from PXRD upon cooling from 300 to 100 K for core and shell components of (left) the 122 nm cores series (4@15, 29, 52-nm), and (right) the 325 nm cores series (2@27, 69, 108-nm).

magnetic data, the shell strain induced by the core is shell-thickness-dependent for shells thinner than the strain depth. Similarly, the results from the Δa versus shell thickness plots in Figure 8 show that for $t < l_{\text{SR}}$, the degree of structural strain does indeed change with shell thickness. Further, the linewidth of the PXRD diffraction peaks can be used to construct a Williamson–Hall plot for each sample, which uses the different scattering angle dependences of localized (e.g., grain boundaries) and delocalized (e.g., strain gradients) defects to deconvolute their effects on the peak width.^{64–67}

$$\frac{H \cos \theta}{\lambda} = \varepsilon \times \frac{2 \sin \theta}{\lambda} + \frac{1}{L_c}, \quad (5)$$

where H is the full-width at half-maximum for the (hkl) reflection peak, θ is the scattering angle, λ is the wavelength of the scattered radiation, L_c is the real-space crystallite size along the (hkl) reciprocal lattice vector, and ε is the microstrain, also along the (hkl) reciprocal lattice vector. Microstrain refers to the distribution of the d -spacings present in the sample. This microstrain is plotted versus shell thickness in Figure S15 for each of the series (details and fits to eq 5 in Supporting Information). Both the small- and medium-core series have data points for shell thicknesses near 30 nm which can be compared. For the smaller cores, this point is near the baseline, while for the medium cores this point is well above the baseline, showing the structural strain, like the decrease in magnetization, propagates through the shell to greater depths with larger cores.

The data plots for the two thinnest shells in Figure 6 showed that the value of $\Delta M_{\text{shell}}^{\text{PMS}}$ changes with shell thickness, even within the strained region, reducing in magnitude for thicker shells. As discussed earlier, for Δa of the shell in Figure 8, the degree of strain in the shell is also reduced in the thicker shells. To establish that these changes in $\Delta M_{\text{shell}}^{\text{PMS}}$ are caused by the changing degree of strain in the shell, the rate of changes in $\Delta M_{\text{shell}}^{\text{PMS}}$ and Δa with increasing shell thickness for the two core sizes shown in Figure 8 were compared. A quantitative basis for this comparison comes from defining “characteristic volumes,” describing the strain decay in terms of the rate that $\Delta M_{\text{shell}}^{\text{PMS}}$ and Δa approach their “thick-shell” limit for each of the core sizes, depicted graphically and explained in Figure S10. For the magnetic data, the characteristic volume is determined from the normalized rate at which $\Delta M_{\text{shell}}^{\text{PMS}}$ changes with increasing shell volume within the strained region, $|\Delta V / \Delta(\Delta M / \Delta M_2)|$. Here, the strain gradient is estimated from the two thinnest shells from each series, using the nomenclature $\Delta M = \Delta M_{\text{shell}}^{\text{PMS}}$ for the thinnest shell and $\Delta M_2 = \Delta M_{\text{shell}}^{\text{PMS}}$ for the medium-shell. This medium-shell thickness serves to approximate the strain

depth. The same approach can be used to determine a characteristic volume for the structural strain, $|\Delta V / \Delta(\Delta a / \Delta a_2)|$, using the medium-shell value for Δa_2 .

Comparisons of these characteristic volumes, $|\Delta V / \Delta(\Delta M / \Delta M_2)|$ and $|\Delta V / \Delta(\Delta a / \Delta a_2)|$, are presented for the small- and medium-core series in Table 2. Both quantities describe how

Table 2. Characterization of the Strain Gradient by Magnetic and Structural Characteristic Volumes

core size	$ \Delta V / \Delta(\Delta M / \Delta M_2) ^a$ (nm ³)	$ \Delta V / \Delta(\Delta a / \Delta a_2) ^b$ (nm ³)
medium, 325 nm	8.3×10^{7d}	7.2×10^{7d}
small, ≈ 124 nm ^c	4.8×10^{6e}	1.7×10^{6f}

^a ΔV is the difference in shell volume between the two thinnest shells of each series, and $\Delta(\Delta M / \Delta M_2)$ denotes the change in $\Delta M_{\text{shell}}^{\text{PMS}}$ over this change in volume divided by $\Delta M_{\text{shell}}^{\text{PMS}}$ evaluated for the medium-shell thickness. ^b ΔV is the difference in shell volume between the two thinnest shells of each series, and $\Delta(\Delta a / \Delta a_2)$ denotes the change in the CTIST-induced Δa of the shell over this change in volume divided by Δa for the medium-shell thickness. ^cTwo similar sets of samples were used in the magnetometry and PXRD experiments on the “small” core size. ^dFrom Samples 2@(27,69-nm). ^eFrom Samples 1@(19, 33-nm). ^fFrom Samples 4@(15, 29-nm).

quickly the respective phenomena asymptote to their constant thick-shell values and thus measure the correlation between the changing degree of strain and the variation in $\Delta M_{\text{shell}}^{\text{PMS}}$ with increasing shell thickness. Table 2 shows that the characteristic volume in terms of $\Delta M_{\text{shell}}^{\text{PMS}}$ is 20 times larger in the medium cores relative to the small cores. The medium-cores series also exhibits a characteristic volume in terms of Δa , which is 40 times that for the small cores, providing strong support that the gradient in $\Delta M_{\text{shell}}^{\text{PMS}}$ directly results from a structural strain gradient. This result is not entirely unexpected: for the small cores, a given change in shell volume increases the thickness of the shell much more than for the medium cores, resulting in a more rapid stiffening of the shell, and therefore a smaller characteristic volume. It is important to note that the cores are transitioning completely in all cases (see Supporting Information), but the stiffening of the shell leads to a smaller degree of strain for thick shells. For the thin-shell samples, the presence of a free surface within the strained region leads to contributions from the image field^{68,69} that do not exist in the thickest shells, which explains why V_{SR} scales with V_{core} for thick-shell samples, despite the demonstrated difference in thin-shell strain profiles.

These observations of a core–shell system with a changing degree of strain in the shell due to increasing shell thickness, approaching a constant value at and beyond the strain depth,

also agree well with the results of theoretical modeling of core–shell spin-transition nanoparticles using continuum mechanics.³² Since continuum mechanics does not take into consideration the discrete nature of the interface which leads to lattice-mismatch effects, the agreement between the observations made in the present study and the strain depth behavior modeled by Félix et al.³² suggests that the most important consideration for determining the strain depth in these heterostructures is the “negative pressure” created by the volume mismatch of the core after the HS-to-LS transition. This pressure is directly proportional to the volume of the core in our case,⁶⁸ and explains the linearity of V_{SR} with respect to V_{core} . This demonstrated applicability of continuum mechanics also shows one advantage of working at the mesoscale, where both classical and quantum phenomena can coexist.^{44,70,71}

Implications for Related Systems. The finite range for the dependence of the strain depth on shell thickness likely has consequences for an important spin-transition heterostructure morphology, spin-transition particles dispersed in a matrix.^{72–75} The results indicate that such a heterostructure cannot be expected to act as a simple sum of single particles in a matrix when local or global particle loading concentrations make the interparticle distances smaller than the sum of the strain depths. This result agrees with the findings of Raza et al.,⁷³ who studied interparticle interactions in SCO platelets with thin silica shells, but left questions about the role of the chemical bonding at the surface. Our results utilizing a system with a constant interface support the conclusion that in the case of short interparticle distances, the particles are expected to show cooperative effects, mediated by the strain induced in the matrix, likely altering the nature of the spin transition.³²

CONCLUSIONS

The response of core–shell particles with a strain-actuating spin-transition core and a magnetic shell can be reasonably described by considering the heterostructure as comprised of three components, the switchable core, a strained region in the shell at the interface with the core, and shell material unaffected by expansion and contraction of the core. By applying this model to a series of chemically similar core–shell particles covering a range of dimensions and core:shell ratios, a linear relationship between the volume of the switchable core and the maximum volume of the strained region in the shell is clearly revealed in magnetic and structural properties. In the examples studied here, it is striking that the magnetic KNiCr-PBA shell is influenced to depths greater than 100 nm in response to the spin transition of the RbCoFe-PBA core. For thin shells, the behavior is more interesting. The extent of strain in the shell depends on the shell thickness, with maximum strain for the thinnest shells that decreases as the shell approaches the limiting strained-region thickness. The nonlinear response in this region is a consequence of feedback between the shell and the actuating core. The stiffness of the shell increases as it becomes thicker, so thin shells are more compressible than thick shells. At the same time, the volume change of the spin-transition core is altered by the elastic characteristics of the shell, decreasing as the shell becomes stiffer. The results have implications for using spin-transitions materials to dynamically induce strain in overlayers and in heterostructures, or as components in composite matrices, for example, as elements for converting light to work.

ASSOCIATED CONTENT

Supporting Information

The Supporting Information is available free of charge at <https://pubs.acs.org/doi/10.1021/acs.chemmater.0c03608>.

Additional details regarding synthetic conditions and characterization protocols, complete sets of magnetic and structural data for all samples, Williamson–Hall plots (PDF)

AUTHOR INFORMATION

Corresponding Authors

Mark W. Meisel – Department of Physics and National High Magnetic Field Laboratory, University of Florida, Gainesville, Florida 32611-8440, United States; orcid.org/0000-0003-4980-5427; Email: meisel@phys.ufl.edu

Daniel R. Talham – Department of Chemistry, University of Florida, Gainesville, Florida 32611-7200, United States; orcid.org/0000-0003-1783-5285; Email: talham@chem.ufl.edu

Authors

John M. Cain – Department of Chemistry, University of Florida, Gainesville, Florida 32611-7200, United States

Ashley C. Felts – Department of Chemistry, University of Florida, Gainesville, Florida 32611-7200, United States

Complete contact information is available at: <https://pubs.acs.org/10.1021/acs.chemmater.0c03608>

Notes

The authors declare no competing financial interest.

ACKNOWLEDGMENTS

This work was supported, in part, by the Division of Materials Research (DMR) at the National Science Foundation (NSF) via DMR-1904596 (D.R.T.), DMR-1708410 (M.W.M.), and DMR-1644779 (National High Magnetic Field Laboratory). This research used Beamline 17-BM of the Advanced Photon Source, a U.S. Department of Energy (DOE) Office of Science User Facility operated for the DOE Office of Science by Argonne National Laboratory under Contract No. DE-AC02-06CH11357.

REFERENCES

- (1) Narayan, A. Class of Rashba Ferroelectrics in Hexagonal Semiconductors. *Phys. Rev. B* **2015**, *92*, 220101.
- (2) Liu, S.; Kim, Y.; Tan, L. Z.; Rappe, A. M. Strain-Induced Ferroelectric Topological Insulator. *Nano Lett.* **2016**, *16*, 1663–1668.
- (3) Yalameha, S.; Nourbakhsh, Z.; Vaez, A. Hydrostatic Strain-Induced Topological Phase of KNa_2Sb . *J. Magn. Magn. Mater.* **2018**, *468*, 279–286.
- (4) Monserrat, B.; Bennett, J. W.; Rabe, K. M.; Vanderbilt, D. Antiferroelectric Topological Insulators in Orthorhombic AMgBi Compounds ($A = \text{Li, Na, K}$). *Phys. Rev. Lett.* **2017**, *119*, No. 036802.
- (5) Manzeli, S.; Ovchinnikov, D.; Pasquier, D.; Yazyev, O. V.; Kis, A. 2D Transition Metal Dichalcogenides. *Nat. Rev. Mater.* **2017**, *2*, 17033.
- (6) Li, X.; Zhang, S.; Wang, Q. Topological Insulating States in 2D Transition Metal Dichalcogenides Induced by Defects and Strain. *Nanoscale* **2017**, *9*, 562–569.
- (7) Xue, X.-X.; Feng, Y.-X.; Liao, L.; Chen, Q.-J.; Wang, D.; Tang, L.-M.; Chen, K. Strain Tuning of Electronic Properties of Various Dimension Elemental Tellurium With Broken Screw Symmetry. *J. Phys.: Condens. Matter* **2018**, *30*, 125001.

- (8) Jiang, X. X.; Feng, Y. X.; Chen, K. Q.; Tang, L. M. The Coexistence of Ferroelectricity and Topological Phase Transition in Monolayer α - In_2Se_3 Under Strain Engineering. *J. Phys.: Condens. Matter* **2020**, *32*, 105501.
- (9) Webster, L.; Yan, J.-A. Strain-Tunable Magnetic Anisotropy in Monolayer CrCl_3 , CrBr_3 , and CrI_3 . *Phys. Rev. B* **2018**, *98*, 144411.
- (10) Goel, S.; Anh, L. D.; Ohya, S.; Tanaka, M. Ferromagnetic Resonance and Control of Magnetic Anisotropy by Epitaxial Strain in the Ferromagnetic Semiconductor ($\text{Ga}_{0.8}\text{Fe}_{0.2}$)Sb at Room Temperature. *Phys. Rev. B* **2019**, *99*, No. 014431.
- (11) Lu, X.-Z.; Rondinelli, J. M. Epitaxial-Strain-Induced Polar-to-Nonpolar Transitions in Layered Oxides. *Nat. Mater.* **2016**, *15*, 951–955.
- (12) Zhu, T.; Li, J. Ultra-Strength Materials. *Prog. Mater. Sci.* **2010**, *55*, 710–757.
- (13) Ghadimi, A. H.; Fedorov, S. A.; Engelsen, N. J.; Bereyhi, M. J.; Schilling, R.; Wilson, D. J.; Kippenberg, T. J. Elastic Strain Engineering for Ultralow Mechanical Dissipation. *Science* **2018**, *360*, 764–768.
- (14) Feng, J.; Qian, X.; Huang, C.-W.; Li, J. Strain-Engineered Artificial Atom as a Broad-Spectrum Solar Energy Funnel. *Nat. Photonics* **2012**, *6*, 866–872.
- (15) He, K.; Poole, C.; Mak, K. F.; Shan, J. Experimental Demonstration of Continuous Electronic Structure Tuning via Strain in Atomically Thin MoS_2 . *Nano Lett.* **2013**, *13*, 2931–2936.
- (16) Zeng, M.; Liu, J.; Zhou, L.; Mendes, R. G.; Dong, Y.; Zhang, M.-Y.; Cui, Z.-H.; Cai, Z.; Zhang, Z.; Zhu, D.; Yang, T.; Li, X.; Wang, J.; Zhao, L.; Chen, G.; Jiang, H.; Rümmler, M.; Zhou, H.; Fu, L. Bandgap Tuning of Two-Dimensional Materials by Sphere Diameter Engineering. *Nat. Mater.* **2020**, *19*, 528–533.
- (17) Leppert, L.; Reyes-Lillo, S. E.; Neaton, J. B. Electric Field- and Strain-Induced Rashba Effect in Hybrid Halide Perovskites. *J. Phys. Chem. Lett.* **2016**, *7*, 3683–3689.
- (18) Berdiyrov, G. R.; Carignano, M. A.; Madjet, M. E. Effect of Hydrostatic Strain on the Electronic Transport Properties of CsPbI_3 . *Comput. Mater. Sci.* **2017**, *137*, 314–317.
- (19) Tholen, H. M. G. A.; Wildmann, J. S.; Rastelli, A.; Trotta, R.; Pryor, C. E.; Zallo, E.; Schmidt, O. G.; Koenraad, P. M.; Silov, A. Y. Active Tuning of the g -Tensor in InGaAs/GaAs Quantum Dots via Strain. *Phys. Rev. B* **2019**, *99*, 195305.
- (20) Shepherd, H. J.; Gural'skiy, I. Y. A.; Quintero, C. M.; Tricard, S.; Salmon, L.; Molnár, G.; Bousseksou, A. Molecular Actuators Driven by Cooperative Spin-State Switching. *Nat. Commun.* **2013**, *4*, 2607.
- (21) Dia, N.; Lisnard, L.; Prado, Y.; Gloter, A.; Stéphan, O.; Brisset, F.; Hafez, H.; Saad, Z.; Mathonière, C.; Catala, L.; Mallah, T. Synergy in Photomagnetic/Ferromagnetic Sub-50 nm Core-Multishell Nanoparticles. *Inorg. Chem.* **2013**, *52*, 10264–10274.
- (22) Gural'skiy, I. Y. A.; Quintero, C. M.; Costa, J. S.; Demont, P.; Molnár, G.; Salmon, L.; Shepherd, H. J.; Bousseksou, A. Spin Crossover Composite Materials for Electrothermomechanical Actuators. *J. Mater. Chem. C* **2014**, *2*, 2949–2955.
- (23) Koo, Y.-S.; Galán-Mascarós, J. R. Spin Crossover Probes Confer Multistability to Organic Conducting Polymers. *Adv. Mater.* **2014**, *26*, 6785–6789.
- (24) Presle, M.; Maurin, I.; Maroun, F.; Cortès, R.; Lu, L.; Sayed Hassan, R.; Larquet, E.; Guigner, J.-M.; Rivière, E.; Wright, J. P.; Boilot, J.-P.; Gacoin, T. Photostrictive/ Piezomagnetic Core–Shell Particles Based on Prussian Blue Analogues: Evidence for Confinement Effects? *J. Phys. Chem. C* **2014**, *118*, 13186–13195.
- (25) Chen, Y. C.; Meng, Y.; Ni, Z. P.; Tong, M. L. Synergistic Electrical Bistability in a Conductive Spin Crossover Heterostructure. *J. Mater. Chem. C* **2015**, *3*, 945–949.
- (26) Suleimanov, I.; Kraieva, O.; Costa, J. S.; Fritsky, I. O.; Molnar, G.; Salmon, L.; Bousseksou, A. Electronic Communication Between Fluorescent Pyrene Excimers and Spin Crossover Complexes in Nanocomposite Particles. *J. Mater. Chem. C* **2015**, *3*, 5026–5032.
- (27) Mikolasek, M.; Manrique-Juarez, M. D.; Shepherd, H. J.; Ridier, K.; Rat, S.; Shalabaeva, V.; Bas, A.-C.; Collings, I. E.; Mathieu, F.; Cacheux, J.; Leichle, T.; Nicu, L.; Nicolazzi, W.; Salmon, L.; Molnár, G.; Bousseksou, A. Complete Set of Elastic Moduli of a Spin-Crossover Solid: Spin-State Dependence and Mechanical Actuation. *J. Am. Chem. Soc.* **2018**, *140*, 8970–8979.
- (28) Liu, K.; Cheng, C.; Cheng, Z. T.; Wang, K. V.; Ramesh, R.; Wu, J. Q. Giant-Amplitude, High-Work Density Microactuators With Phase Transition Activated Nanolayer Bimorphs. *Nano Lett.* **2012**, *12*, 6302–6308.
- (29) Asakura, D.; Li, C. H.; Mizuno, Y.; Okubo, M.; Zhou, H.; Talham, D. R. Bimetallic Cyanide-Bridged Coordination Polymers as Lithium Ion Cathode Materials: Core@Shell Nanoparticles With Enhanced Cyclability. *J. Am. Chem. Soc.* **2013**, *135*, 2793–2799.
- (30) Felts, A. C.; Slimani, A.; Cain, J. M.; Andrus, M. J.; Ahir, A. R.; Abboud, K. A.; Meisel, M. W.; Boukhedaden, K.; Talham, D. R. Control of the Speed of a Light-Induced Spin Transition Through Mesoscale Core–Shell Architecture. *J. Am. Chem. Soc.* **2018**, *140*, 5814–5824.
- (31) Wu, F.; Fitzhugh, W.; Ye, L.; Ning, J.; Li, X. Advanced Sulfide Solid Electrolyte by Core-Shell Structural Design. *Nat. Commun.* **2018**, *9*, 4037.
- (32) Félix, G.; Mikolasek, M.; Molnár, G.; Nicolazzi, W.; Bousseksou, A. Control of the Phase Stability in Spin-Crossover Core-Shell Nanoparticles Through the Elastic Interface Energy. *Eur. J. Inorg. Chem.* **2018**, 435–442.
- (33) Adam, A.; Poggi, M.; Larquet, E.; Cortès, R.; Martinelli, L.; Coulon, P.-E.; Lahera, E.; Proux, O.; Chernyshov, D.; Boukhedaden, K.; Gacoin, T.; Maurin, I. Strain Engineering of Photo-Induced Phase Transformations in Prussian Blue Analogue Heterostructures. *Nanoscale* **2018**, *10*, 16030–16039.
- (34) Ijiri, Y.; Krycka, K. L.; Hunt-Isaak, I.; Pan, H.; Hsieh, J.; Borchers, J. A.; Rhyne, J. J.; Oberdick, S. D.; Abdelgawad, A.; Majetich, S. A. Correlated Spin Canting in Ordered Core-Shell $\text{Fe}_3\text{O}_4/\text{Mn}_x\text{Fe}_{3-x}\text{O}_4$ Nanoparticle Assemblies. *Phys. Rev. B* **2019**, *99*, No. 094421.
- (35) Landau, L. D.; Lifšic, E. M. *Theory of elasticity*. Elsevier: Amsterdam, 2008.
- (36) Kawamoto, T.; Abe, S. Thermal Hysteresis Loop of the Spin-State in Nanoparticles of Transition Metal Complexes: Monte Carlo Simulations on an Ising-Like Model. *Chem. Commun.* **2005**, 3933–3935.
- (37) Stoleriu, L.; Chakraborty, P.; Hauser, A.; Stancu, A.; Enachescu, C. Thermal Hysteresis in Spin-Crossover Compounds Studied Within the Mechanoelastic Model and its Potential Application to Nanoparticles. *Phys. Rev. B* **2011**, *84*, 134102.
- (38) Oubouchou, H.; Slimani, A.; Boukhedaden, K. Interplay Between Elastic Interactions in a Core-Shell Model for Spin-Crossover Nanoparticles. *Phys. Rev. B* **2013**, *87*, 104104.
- (39) Peng, H.; Tricard, S.; Félix, G.; Molnár, G.; Nicolazzi, W.; Salmon, L.; Bousseksou, A. Re-Appearance of Cooperativity in Ultra-Small Spin-Crossover $[\text{Fe}(\text{pz})\{\text{Ni}(\text{CN})_4\}]$ Nanoparticles. *Angew. Chem., Int. Ed.* **2014**, *126*, 11074–11078.
- (40) Linares, J.; Jureschi, C.; Boukhedaden, K. Surface Effects Leading to Unusual Size Dependence of the Thermal Hysteresis Behavior in Spin-Crossover Nanoparticles. *Magnetochemistry* **2016**, *2*, 24.
- (41) Ridier, K.; Bas, A. C.; Shalabaeva, V.; Nicolazzi, W.; Salmon, L.; Molnár, G.; Bousseksou, A.; Lorenc, M.; Bertoni, R.; Collet, E.; Cailleau, H. Finite Size Effects on the Switching Dynamics of Spin-Crossover Thin Films Photoexcited by a Femtosecond Laser Pulse. *Adv. Mater.* **2019**, *31*, 1901361.
- (42) Matthews, J. W.; Blakeslee, A. E.; Mader, S. Use of Misfit Strain to Remove Dislocations From Epitaxial Thin Films. *Thin Solid Films* **1976**, *33*, 253–266.
- (43) Cammarata, R. C. Surface and Interface Stress Effects in Thin Films. *Prog. Surf. Sci.* **1994**, *46*, 1–38.
- (44) Risset, O. N.; Talham, D. R. Effects of Lattice Misfit on the Growth of Coordination Polymer Heterostructures. *Chem. Mater.* **2015**, *27*, 3838–3843.

- (45) Catala, L.; Brinzei, D.; Prado, Y.; Gloter, A.; Stéphan, O.; Rogez, G.; Mallah, T. Core-Multishell Magnetic Coordination Nanoparticles: Toward Multifunctionality on the Nanoscale. *Angew. Chem., Int. Ed.* **2009**, *48*, 183–187.
- (46) Andrus, M. J.; Calm, Y. M.; Knowles, E. S.; Dumont, M. F.; Abboud, K. A.; Meisel, M. W.; Talham, D. R. Influence of Particle Size on the Phase Behavior Associated With the Thermal Spin Transition of the Prussian Blue Analogue $K_{0.4}Co_{1.3}[Fe(CN)_6] \cdot 4.4H_2O$. *Polyhedron* **2013**, *64*, 289–293.
- (47) Risset, O. N.; Quintero, P. A.; Brinzari, T. V.; Andrus, M. J.; Lufaso, M. W.; Meisel, M. W.; Talham, D. R. Light-Induced Changes in Magnetism in a Coordination Polymer Heterostructure, $Rb_{0.24}Co[Fe(CN)_6]_{0.74}@K_{0.10}Co[Cr(CN)_6]_{0.70} \cdot nH_2O$ and the Role of the Shell Thickness on the Properties of Both Core and Shell. *J. Am. Chem. Soc.* **2014**, *136*, 15660–15669.
- (48) Sato, O.; Iyoda, T.; Fujishima, A.; Hashimoto, K. Photoinduced Magnetization of a Cobalt-Iron Cyanide. *Science* **1996**, *272*, 704–705.
- (49) Sato, O.; Einaga, Y.; Fujishima, A.; Hashimoto, K. Photoinduced Long-Range Magnetic Ordering of a Cobalt-Iron Cyanide. *Inorg. Chem.* **1999**, *38*, 4405–4412.
- (50) Létard, J.-F.; Chiara, C.; Courcot, E.; Costa, J. S. A Typical Example of a Photomagnetic Study Carried Out on a Spin-Crossover Material. *Bull. Mater. Sci.* **2006**, *29*, S67–S71.
- (51) Zentková, M.; Arnold, Z.; Kamarád, J.; Kavečanský, V.; Lukáčová, M.; Mat'áš, S.; Mihalik, M.; Mitróová, Z.; Zentko, A. Effect of Pressure on the Magnetic Properties of $Tm_3[Cr(CN)_6]_2 \cdot 12H_2O$. *J. Phys.: Condens. Matter* **2007**, *19*, 266217.
- (52) Bigelow, J. H.; Bailar, J. C. Potassium Hexacyanochromate(III). In *Inorg. Synth.*; Fernelius, W. C., Ed; John Wiley & Sons, Inc.: Hoboken, NJ, USA, 2007.
- (53) Felts, A. C.; Andrus, M. J.; Averback, C. M.; Li, C. H.; Talham, D. R. Comparison of the Infrared Absorptivities of Some Prussian Blue Analogues and Their Use to Determine the Composition of Core-Shell Particles. *Polyhedron* **2017**, *133*, 404–411.
- (54) Schneider, C. A.; Rasband, W. S.; Eliceiri, K. W. NIH Image to ImageJ: 25 years of image analysis. *Nat. Methods* **2012**, *9*, 671–675.
- (55) Toby, B. H.; Von Dreele, R. B. GSAS-II: the Genesis of a Modern Open-Source All Purpose Crystallography Software Package. *J. Appl. Crystallogr.* **2013**, *46*, 544–549.
- (56) Rodríguez-Carvajal, J. FULLPROF: A Program for Rietveld Refinement and Pattern Matching Analysis. *Powder Diffr.* **1990**, *15*, 127.
- (57) Pejakovic, D. A.; Manson, J. L.; Miller, J. S.; Epstein, A. J. Cluster Glass State and Photoinduced Effects on the Freezing Dynamics in $K_xCo[Fe(CN)_6]_y \cdot zH_2O$ ($x \sim 0.16$, $y \sim 0.72$, $z \sim 4.4$). *J. Appl. Phys.* **2000**, *87*, 6028–6030.
- (58) Felts, A. C.; Andrus, M. J.; Knowles, E. S.; Quintero, P. A.; Ahir, A. R.; Risset, O. N.; Li, C. H.; Maurin, I.; Halder, G. J.; Abboud, K. A.; Meisel, M. W.; Talham, D. R. Evidence for Interface-Induced Strain and its Influence on Photomagnetism in Prussian Blue Analogue Core-Shell Heterostructures, $Rb_aCo_b[Fe(CN)_6]_c \cdot mH_2O @ K_nNi_k[Cr(CN)_6]_l \cdot nH_2O$. *J. Phys. Chem. C* **2016**, *120*, 5420–5429.
- (59) Fitta, M.; Prima-Garcia, H.; Czaja, P.; Korzeniak, T.; Krupiński, M.; Wojtyniak, M.; Bałanda, M. Magnetic and Magneto-Optical Properties of Nickel Hexacyanoferrate/Chromate Thin Films. *RSC Adv.* **2017**, *7*, 1382–1386.
- (60) Gros, C. R.; Peparah, M. K.; Felts, A. C.; Brinzari, T. V.; Risset, O. N.; Cain, J. M.; Ferreira, C. F.; Meisel, M. W.; Talham, D. R. Synergistic Photomagnetic Effects in Coordination Polymer Heterostructure Particles of Hofmann-Like $Fe(4\text{-phenylpyridine})_2 [Ni(CN)_4] \cdot 0.5H_2O$ and $K_{0.4}Ni[Cr(CN)_6]_{0.8} \cdot nH_2O$. *Dalton Trans.* **2016**, *45*, 16624–16634.
- (61) Knowles, E. S.; Li, C. H.; Dumont, M. F.; Peparah, M. K.; Andrus, M. J.; Talham, D. R.; Meisel, M. W. Photoinduced Perturbations of the Magnetic Superexchange in Core@Shell Prussian Blue Analogues. *Polyhedron* **2013**, *66*, 153–156.
- (62) Quintero, P. A. Magnetic and Electrical Transport Studies of Molecule-Based Magnets. Ph.D. Dissertation, University of Florida, Gainesville, FL, 2015.
- (63) Ahir, A. R. Structural Analysis of Heterostructured Core-Shell Prussian Blue Analogues to Study Interfacial Synergistic Effects in Thermal Expansion. Ph.D. Dissertation, University of Florida, Gainesville, FL, 2016.
- (64) Williamson, G. K.; Hall, W. H. X-Ray Line Broadening From Filled Aluminium and Wolfram. *Acta Metall.* **1953**, *1*, 22–31.
- (65) van Berkum, J. G. M.; Delhez, R.; de Keijser, T. H.; Mittemeijer, E. J. Diffraction-Line Broadening Due to Strain Fields in Materials; Fundamental Aspects and Methods of Analysis. *Acta Crystallogr., Sect. A: Found. Crystallogr.* **1996**, *52*, 730–747.
- (66) Scardi, P.; Leoni, M.; Delhez, R. Line Broadening Analysis Using Integral Breadth Methods: a Critical Review. *J. Appl. Crystallogr.* **2004**, *37*, 381–390.
- (67) Thompson, P.; Cox, D. E.; Hastings, J. B. Rietveld Refinement of Debye-Scherrer Synchrotron X-ray Data From Al_2O_3 . *J. Appl. Crystallogr.* **1987**, *20*, 79–83.
- (68) Eshelby, J. D. The Continuum Theory of Lattice Defects. In *Solid State Physics*; Seitz, F.; Turnbull, D., Eds.; Academic Press, 1956; *3*; 79–144.
- (69) Boukheddaden, K. Monte Carlo Investigations on Surface Elastic Energy of Spin-Crossover Solids: Direct Access to Image Pressure and the Eshelby Constant. *Phys. Rev. B* **2013**, *88*, 134105.
- (70) Corrales, S. A.; Cain, J. M.; Uhlig, K. A.; Mowson, A. M.; Papatriantafyllopoulou, C.; Peparah, M. K.; Ozarowski, A.; Tasiopoulos, A. J.; Christou, G.; Meisel, M. W.; Lampropoulos, C. Introducing Dimensionality to the Archetypal Mn_{12} Single-Molecule Magnet: a Family of $[Mn_{12}]_n$ Chains. *Inorg. Chem.* **2016**, *55*, 1367–1369.
- (71) Volkov, O. M.; Sheka, D. D.; Gaididei, Y.; Kravchuk, V. P.; Röblier, U. K.; Fassbender, J.; Makarov, D. Mesoscale Dzyaloshinskii-Moriya Interaction: Geometrical Tailoring of the Magnetochirality. *Sci. Rep.* **2018**, *8*, 866.
- (72) Tissot, A.; Bardeau, J.-F.; Rivière, E.; Brisset, F.; Boillot, M.-L. Thermo- and Photoswitchable Spin-Crossover Nanoparticles of an Iron(II) Complex Trapped in Transparent Silica Thin Films. *Dalton Trans.* **2010**, *39*, 7806.
- (73) Raza, Y.; Volatron, F.; Moldovan, S.; Ersen, O.; Huc, V.; Martini, C.; Brisset, F.; Gloter, A.; Stéphan, O.; Bousseksou, A.; Catala, L.; Mallah, T. Matrix-Dependent Cooperativity in Spin Crossover $Fe(pyrazine)Pt(CN)_4$ Nanoparticles. *Chem. Commun.* **2011**, *47*, 11501.
- (74) Durand, P.; Pillet, S.; Bendeif, E.-E.; Carteret, C.; Bouazaoui, M.; El Hamzaoui, H.; Capoen, B.; Salmon, L.; Hébert, S.; Ghanbaja, J.; Aranda, L.; Schaniel, D. Room Temperature Bistability With Wide Thermal Hysteresis in a Spin Crossover Silica Nanocomposite. *J. Mater. Chem. C* **2013**, *1*, 1933.
- (75) Zhao, T.; Cuignet, L.; Dêrtu, M. M.; Wolff, M.; Spasojevic, V.; Boldog, I.; Rotaru, A.; Garcia, Y.; Janiak, C. Water Effect on the Spin-Transition Behavior of Fe(II) 1,2,4-triazole 1D Chains Embedded in Pores of MCM-41. *J. Mater. Chem. C* **2015**, *3*, 7802–7812.